ELSEVIER

Barotropic tides in the Bab el Mandab Strait—numerical simulations

E. Jarosz[a,*], C.A. Blain[b], S.P. Murray[a,1], M. Inoue[a]

[a]*Coastal Studies Institute, Louisiana State University, Baton Rouge, LA 70803, USA*
[b]*Naval Research Laboratory, Stennis Space Center, MS 39529, USA*

Abstract

A two-dimensional barotropic finite element model with the grid resolution varying between 0.2 and 2 km and forced by eight principle constituents (Q_1, O_1, P_1, K_1, N_2, M_2, S_2, and K_2) was used to compute tidal elevations and currents in the Bab el Mandab Strait. Good agreement is achieved with the available observations for both diurnal and semidiurnal tidal currents and diurnal elevations; however, the model performs less satisfactorily for the semidiurnal elevations mainly due to the errors between the observed and computed phases in the region where there are amphidromic points for the M_2, S_2, and N_2 constituents in the Strait. The results indicate that the largest amplitudes of the tidal elevations and the strongest currents are present in the southern part of the Strait. Residual circulation induced by the barotropic tides is rather weak in the major part of the Strait, and its contribution to the Red Sea water transport is small. The model results also show that barotropic energy fluxes are not very large and their direction depends on the constituent. All diurnal and one semidiurnal (N_2) constituent have one major source of energy, which is the flux from the Gulf of Aden, while there are two sources of energy for the M_2, S_2, and K_2 components: one from the Gulf and another from the Red Sea. Very small energy fluxes from the Strait to the adjacent basins indicate that almost all tidal energy is dissipated within the Strait. The distribution of the rate of energy dissipation due to bottom friction implies that the major area of dissipation is located between Perim Narrows and the Assab-Mocha line.
Published by Elsevier Ltd.

Keywords: Barotropic tides; Bab el Mandab Strait; Numerical model; Residual circulation; Tidal energy flux

*Corresponding author. Oceanography Division (Code 7332), Naval Research Laboratory, Stennis Space Center, MS 39529-5004, USA. Tel.: +1 228 688 4292; fax: +1 228 688 4759.

E-mail address: ewa.jarosz@nrlssc.navy.mil (E. Jarosz).

[1]Current affiliation: Office of Naval Research, 800 N. Quincy St., Arlington, VA 22217, USA.

1. Introduction

The Bab el Mandab Strait is located in the southern part of the Red Sea and extends from Perim Island in the south to the Hanish Islands in the northwest (Fig. 1). This Strait is the only
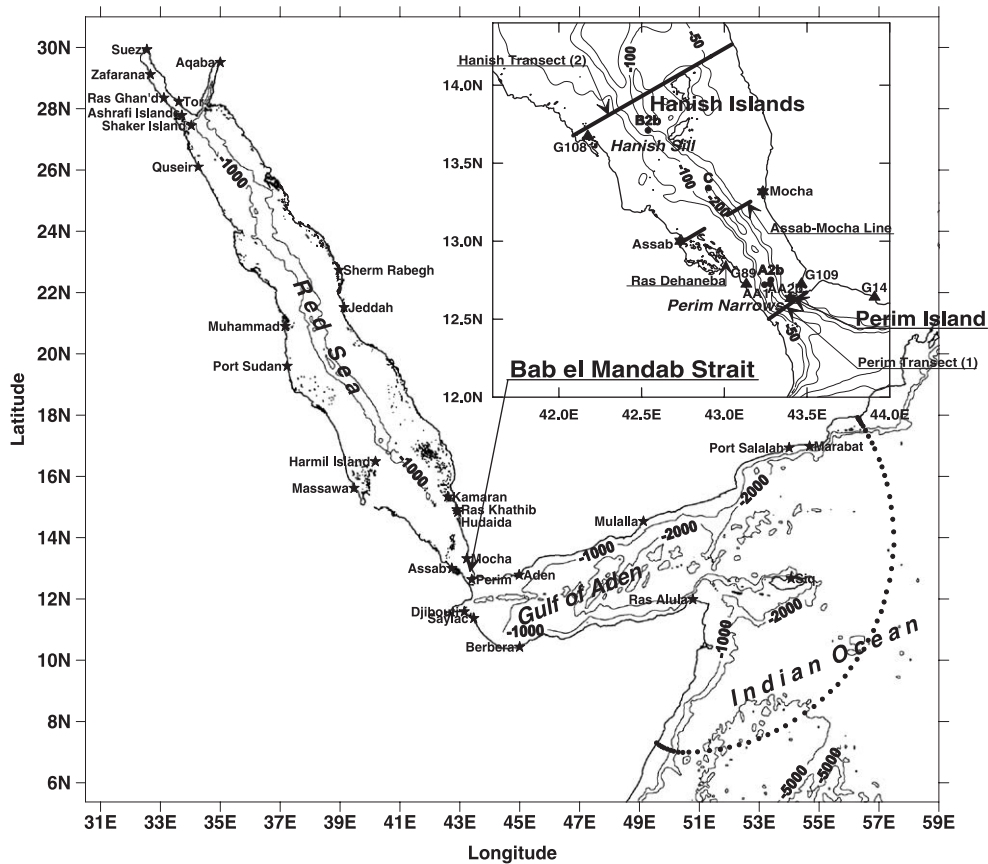
Fig. 1. Map of the Red Sea, Bab el Mandab Strait, Gulf of Aden and north-western Indian Ocean; shown are locations of the water level stations (stars), subsurface pressure gauges (triangles), ADCP moorings (closed circles), Perim and Hanish transects, and open ocean boundary of the model (dotted line); depth contours are in meters.

passage for the Red Sea waters, an important component of the thermohaline circulation in the Indian Ocean, to the Gulf of Aden/Indian Ocean system.

A strong thermohaline exchange flow, which is the most prominent feature of the circulation within the Bab el Mandab Strait, is highly influenced by both synoptic timescale wind forcing and strong tidal motions. This exchange flow exhibits a distinct seasonal variability, and the overall picture emerging from all available investigations is a two-layer winter inverse estuarine (fresh inflow on top of a hypersaline outflow) exchange during October to May, replaced between June and September by a three-layer exchange comprised of a shallow surface outflow,

an intermediate intrusion of the relatively fresh and cold Gulf of Aden Intermediate Waters, and a deep hypersaline outflow which is a small fraction of the winter value (Vercelli, 1931; Thompson, 1939; Smeed, 1997; Murray and Johns, 1997). Recent and historical observations indicate that tidal motion is also a very significant factor of the flow field in the Bab el Mandab Strait (Vercelli, 1925, 1927; Siedler, 1969; Jarosz, 2002). The tidal elevations and currents there exhibit strong diurnal and semidiurnal oscillations. Barotropic tides dominate in this Strait, while baroclinic tides, which are more prominent for the winter exchange flow period and primarily of a diurnal period, are less energetic (Jarosz, 2002). The strongest internal tidal fluctuations are confined to a pycnocline

layer, i.e. to depths within the water column where the greatest density gradients are observed. In addition, analyses of historical data led to the conclusion that there is an amphidrome for the M_2 tidal wave in the Bab el Mandab Strait (Vercelli, 1925; Defant, 1961).

The available observations, however, are spatially scattered and too sparse to examine tidal dynamics in the Bab el Mandab Strait in more detail. It is rather difficult with these data to conclude, for instance, whether there are also amphidromic points for other major tidal constituents and where these points are located. With this data set, it is also difficult to evaluate tidal residual currents, their variability and possible contribution to the transport of the Red Sea waters to the Gulf of Aden/Indian Ocean system or to estimate barotropic tidal energy. To better understand the tidal dynamics in the Bab el Mandab Strait and address some of the posed questions, a numerical model with a very high spatial resolution is implemented. Specific objectives are to (1) quantify the spatial variability of the barotropic tidal elevations and currents in the Bab el Mandab Strait, (2) evaluate the barotropic tidal residual circulation and its contribution to the transport of the Red Sea waters, and (3) estimate the barotropic energy fluxes and dissipation rates for this Strait.

The barotropic tides in the Strait are numerically simulated with a two-dimensional form of the finite element hydrodynamic model called ADvanced CIRCulation Model for Shelves, Coasts and Estuaries (ADCIRC) developed by Luettich et al. (1992) and Westerink et al. (1994). Selection of a finite element model is justified by its grid flexibility, which allows easy incorporation of the complex coastline and high levels of refinement near shallow coastal areas and in regions of rapid bathymetric change. It also permits coarsening of the grid over deeper waters to extend the domain boundaries away from the primary region of interest. Furthermore, finite element models have a history of accuracy in modeling barotropic tides (Walters, 1987; Werner and Lynch, 1987; Walters and Werner, 1989; Westerink et al., 1989, 1992; Foreman et al., 1995).

This paper is organized as follows. In Section 2, the numerical model and finite element mesh is briefly described. Model-data comparisons are presented in Section 3. Variability of tidal elevations and currents are discussed in Section 4. Residual circulation is described in Section 5, with energy fluxes and dissipation rate distribution presented in Section 6. Section 7 summarizes the findings of the study.

2. Model description

The model domain, shown in Fig. 1, includes not only the Bab el Mandab Strait but also the entire Red Sea, Gulf of Aden and northwestern part of the Indian Ocean. Such a large model area was chosen primarily to reproduce tidal waves propagating from the Indian Ocean, which is a major forcing of tidal motion in the Strait and Red Sea as discussed by Defant (1961). A second motivation was to avoid a necessity of having two open boundaries at the northern and southern ends of the Strait. The tidal elevation data outside and within the Strait are limited, thus estimation of the reliable tidal elevation harmonic constants at the open boundaries located near the Strait would be difficult.

Bathymetry for the model was obtained from two sources: the Naval Oceanographic Office Digital Bathymetric Data Base—Variable Resolution (DBDB-V) (NAVOCEANO, 1997) and charts published by the Defense Mapping Agency in 1992. The bathymetry from the charts was digitized, and this data set (of resolution ~0.11′) is limited to an area slightly larger than the Strait itself, while the DBDB-V data with a resolution of 2′ cover the remainder of the model domain.

The finite element grid used in computations is displayed in Fig. 2. It consists of 37,436 nodes and 70,733 elements. Nodal spacing for this mesh varies throughout the modeled region and ranges between 0.2 and 55.5 km with the highest refinement present in the Strait where the minimum and maximum nodal spacing are 0.2 and 2 km, respectively. The coarsest resolution is located in deep waters of the Gulf of Aden and Indian Ocean.
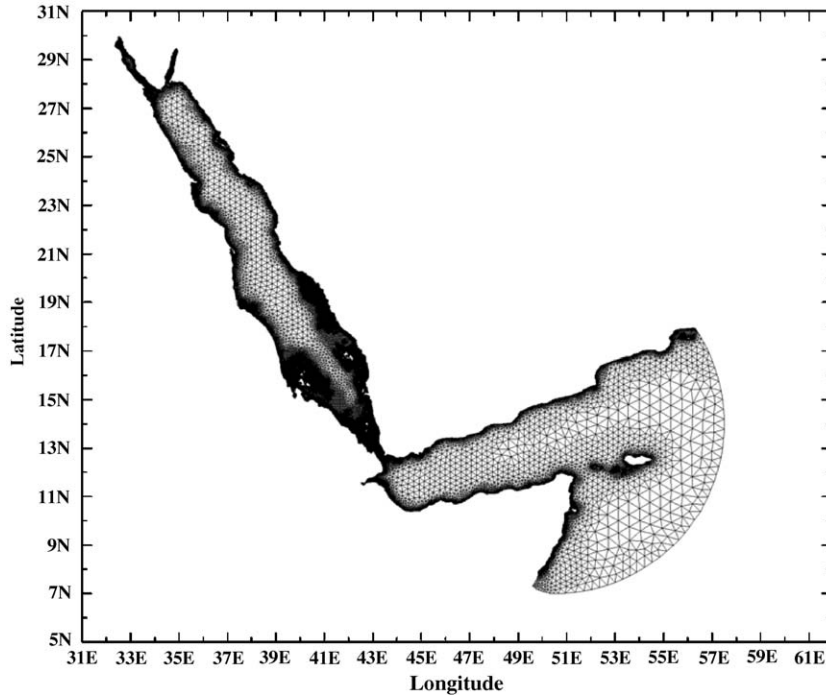
Fig. 2. Model finite element grid.

The two-dimensional form of the ADCIRC model is based on vertically integrated equations of motion and continuity, which, in a spherical coordinate system, are defined as follows (Gill, 1982):

$$\frac{\partial U}{\partial t} + \frac{U}{R\cos\phi}\frac{\partial U}{\partial \lambda} + \frac{V}{R}\frac{\partial U}{\partial \phi} - fV - \frac{UV\sin\phi}{R\cos\phi}$$
$$= -\frac{g}{R\cos\phi}\frac{\partial}{\partial \lambda}(\zeta - \alpha\eta) - \frac{\tau_{b\lambda}}{\rho_0 H} \tag{1a}$$

$$\frac{\partial V}{\partial t} + \frac{U}{R\cos\phi}\frac{\partial V}{\partial \lambda} + \frac{V}{R}\frac{\partial V}{\partial \phi} + fU + \frac{UV\sin\phi}{R\cos\phi}$$
$$= -\frac{g}{R}\frac{\partial}{\partial \phi}(\zeta - \alpha\eta) - \frac{\tau_{b\phi}}{\rho_0 H} \tag{1b}$$

$$\frac{\partial \zeta}{\partial t} + \frac{1}{R\cos\phi}\frac{\partial(UH)}{\partial \lambda} + \frac{1}{R\cos\phi}\frac{\partial(VH\cos\phi)}{\partial \phi} = 0 \tag{1c}$$

where t represents time, λ, φ denote degrees of longitude and latitude, ζ is the free surface elevation, U, V are the depth-averaged horizontal east–west and north–south velocities, respectively, $H = \zeta + h$

is the total water column depth, h is the bathymetric depth relative to the geoid, $f = 2\Omega\sin\varphi$ is the Coriolis parameter, Ω is the angular speed of the Earth, ρ_0 is a reference density, g is the acceleration due to gravity, α is the Earth elasticity factor approximated as 0.69 for all tidal constituents as used by other investigators including Schwiderski (1980) and Hendershott (1981); however, its value has been shown to be constituent-dependent (Wahr, 1981), η is the Newtonian equilibrium tidal potential, and $\tau_{b\lambda}$, $\tau_{b\varphi}$ are the bottom stresses taken as:

$$\tau_{b\lambda} = \rho_0 C_d U\sqrt{U^2 + V^2},$$
$$\tau_{b\phi} = \rho_0 C_d V\sqrt{U^2 + V^2}, \tag{2}$$

where C_d denotes the bottom drag coefficient. The equilibrium tidal potential is expressed as (Reid, 1990)

$$\eta(\lambda, \phi, t) = \sum_{n,j} C_{jn} f_{jn}(t_0) L_j(\phi) \cos[2\pi(t - t_0)/T_{jn}$$
$$+ j\lambda + v_{jn}(t_0)], \tag{3}$$

where t is time relative to t_0, which is the reference time, C_{jn} is a constant characterizing the amplitude of a tidal constituent n of species j, f_{jn} is the time-dependent nodal factor, v_{jn} is the time-dependent astronomical argument, $j = 0, 1, 2$ are the tidal species ($j = 0$ declinational; $j = 1$ diurnal, $j = 2$ semidiurnal), $L_0 = 3\sin^2\varphi - 1$, $L_1 = \sin(2\varphi)$, $L_2 = \cos^2\varphi$, and T_{jn} is the period of a constituent n for species j. The tidal loading and self-attraction are not included in the model equations.

Prior to being discretized, the continuity and momentum equations are combined into a generalized wave continuity equation (GWCE), which has been shown to have superior numerical properties to a primitive continuity equation when a finite element method is used in space (Lynch and Gray, 1979). The final forms of the GWCE and momentum equations, which are solved by the model, are given in Blain and Rogers (1998); while numerical discretization of these equations is described in detail by Luettich et al. (1992) and Kolar et al. (1994).

No-normal flow and free tangential slip conditions are imposed at the land boundary nodes. Furthermore, at the open ocean boundary, the tidal elevation generated by four diurnal (K_1, O_1, P_1, Q_1) and four semidiurnal (M_2, S_2, N_2, K_2) constituents is specified (Dirichlet condition). The tidal harmonic constants used to generate the elevation along the open boundary are linearly interpolated onto the boundary nodes using data from the World Ocean Tide Model database FES95.2 (Le Provost et al., 1994). In addition, an equilibrium tidal potential forcing within the domain is applied for the same eight constituents.

A constant value for the bottom friction coefficient, equal to 0.003, was applied throughout the domain. Several bottom friction coefficients were tried, and the value of 0.003 gave the best agreement with the observations. A time step of 30 s was used to ensure model stability based on the Courant number criterion. The parameter τ_0, which weights the primitive and GWCE form of the continuity equation, was estimated from a formula given by Westerink et al. (1994) and set equal to 0.001. Finally, the minimum depth was assigned to be 2 m to eliminate any potential drying of computational nodes since wetting and drying option is not included in these simulations. The model simulations were carried out for 1 year to generate a long time series that allows the separation of P_1 and K_2 constituents from K_1 and S_2, respectively. The amplitudes and phases of the tidal constituents were obtained through the standard harmonic analysis (Foreman, 1977, 1978).

3. Validation of computed tides

Tidal harmonic constants at 29 water level stations and four subsurface pressure gauges as well as estimates of the barotropic tidal currents obtained from the measurements at five ADCP moorings collected during the project entitled "Observation and Modeling—an Integrated Study of the Transport through the Strait of Bab el Mandab" (the BAM project) (Murray and Johns, 1997) were used to evaluate computed tidal elevations and currents. The ADCP observations were vertically averaged before they were compared to the modeled currents (see Jarosz (2002) for more details regarding pressure gauge and ADCP data processing and analyses). Geographical locations of the water level stations, for which only the tidal harmonic constants were obtained from the International Hydrographic Organization (1979), and pressure gauges, deployed for the BAM project, are listed in Table 1 and displayed in Fig. 1. All observed tidal amplitudes and phases come from near-coastal areas leaving no possibility of verifying the model predictions of the tidal elevations in open waters. In addition, at some water level stations only a few tidal constituents were available for the comparison; the common constituents for all stations were K_1, O_1, M_2, and S_2.

Major features of the diurnal tidal elevations, such as larger amplitudes in the Gulf of Aden and much smaller ones in the Red Sea proper, are qualitatively captured by the model when compared to the available observations (Table 1). Similarly, well represented are major features of the semidiurnal tidal elevations. Such semidiurnal features include higher amplitudes in the Gulf of Aden, Aquaba and Suez, very small M_2

Table 1
Comparison of computed (Com) and observed (Obs) K_1/O_1 and M_2/S_2 amplitudes (A) and phases (g, GMT) at the coastal stations

Station name	Latitude(N)/Longitude(E)	K_1/O_1				M_2/S_2			
		A (cm)		g (°)		A (cm)		g (°)	
		Obs	Com	Obs	Com	Obs	Com	Obs	Com
Aden[a]	12°47′	40.0	39.0	350	346	48.0	49.5	134	133
	44°59′	20.0	20.0	352	350	21.0	21.8	159	148
Aqaba[b]	29°31′	2.0	1.7	158	160	28.0	16.2	128	134
	35°00′	1.0	0.5	146	164	8.0	6.2	155	154
Ashrafi Islands[b]	27°47′	2.0	2.0	167	159	25.0	14.2	118	129
	33°43′	1.0	0.7	153	154	4.0	5.1	145	151
Assab[c]	13°00′	18.0	14.5	335	340	6.9	14.3	259	118
	42°44′	8.5	6.7	344	344	4.0	7.1	170	155
Berbera[a]	10°26′	46.0	38.3	349	348	48.0	49.5	135	134
	45°00′	19.0	19.6	356	351	20.0	21.8	160	161
Djibouti[a]	11°35′	39.0	38.7	354	347	46.3	51.4	139	134
	43°09′	19.0	19.8	357	351	20.5	22.0	163	160
G14[a]	12°38.5′	39.0	38.4	340	348	47.0	50.2	119	133
	43°54.5′	20.0	19.7	344	351	20.0	22.0	139	160
G89[c]	12°43.5′	30.0	27.9	340	346	23.0	34.4	121	131
	43°08′	15.0	14.2	345	349	14.0	15.6	142	160
G109[c]	12°43.6′	30.0	30.0	340	350	29.0	34.0	125	134
	43°28′	15.0	15.2	345	354	16.0	16.7	144	162
G108[c]	13°40.5′	6.0	4.4	321	350	24.0	8.0	286	350
	42°10.5′	2.0	1.5	335	354	5.0	2.0	299	15
Harmil Island[b]	16°29′	2.0	2.0	166	161	13.0	15.0	318	318
	40°11′	1.0	0.7	180	160	3.0	6.4	334	344
Hudaida[b]	14°50′	1.0	1.2	340	27	30.0	13.0	305	320
	42°56′	1.0	0.6	92	104	6.0	4.5	351	341
Jeddah[b]	21°31′	2.8	3.0	156	159	6.0	3.4	109	149
	39°08′	1.0	2.0	161	159	1.0	1.4	132	172
Kamaran[b]	15°20′	2.0	1.0	34	99	33.0	18.0	300	324
	42°36′	1.0	1.0	140	136	9.0	6.9	334	348
Marabat[b]	16°59′	33.0	34.5	345	342	32.0	32.3	144	144
	54°41′	19.0	18.2	346	345	14.0	12.9	170	169
Massawa[b]	15°37′	2.3	2.8	164	166	33.4	34.4	328	333
	39°28′	2.0	2.1	184	163	12.4	15.0	332	3
Mocha[c]	13°19′	7.0	16.0	335	352	8.0	14.0	244	134
	43°14′	6.1	7.8	352	358	4.5	7.2	188	166
Muhammad[b]	20°54′	3.0	2.9	166	160	6.0	2.9	132	176
	37°10′	2.0	1.7	175	159	1.0	1.2	185	210
Mulalla[a]	14°32′	40.0	36.8	349	345	40.0	38.6	136	134
	49°08′	20.0	19.2	352	348	12.0	16.6	164	159
Perim[c]	12°38′	35.0	34.5	350	350	37.0	42.6	136	136
	43°24′	18.0	18.1	351	353	17.0	18.9	159	162
Port Salalah[a]	16°56′	36.0	34.7	344	343	31.0	31.9	144	143
	54°00′	18.0	18.2	347	345	12.0	12.8	168	168
Port Sudan[b]	19°36′	2.0	2.9	168	157	1.0	1.5	204	246
	37°14′	2.0	1.7	170	156	1.0	0.8	256	277
Quseir[b]	26°06′	2.0	2.2	158	154	22.0	13.0	112	134
	34°16′	2.0	1.0	192	153	5.0	4.9	139	156
Ras Alula[a]	11°59′	37.1	35.6	348	356	36.3	36.5	139	138
	50°47′	18.9	18.5	353	350	15.4	15.8	156	163
Ras Ghan'd[b]	28°21′	2.0	2.9	160	163	18.0	9.0	274	302

Table 1 (*continued*)

Station name	Latitude(N)/Longitude(E)	K_1/O_1				M_2/S_2			
		A (cm)		g (°)		A (cm)		g (°)	
		Obs	Com	Obs	Com	Obs	Com	Obs	Com
	33°07′	2.0	0.9	157	154	7.0	3.0	302	318
Ras Khathib[b]	14°55′	4.0	1.2	69	25	26.0	13.0	294	318
	42°54′	1.0	0.6	82	82	7.0	4.5	339	339
Saylac[a]	11°22′	40.0	38.9	348	348	50.0	51.6	137	133
	43°28′	20.0	19.9	356	351	20.0	22.6	153	161
Shaker Island[b]	27°27′	2.0	2.0	167	154	25.0	14.0	117	132
	34°02′	1.0	0.7	178	151	4.0	5.1	144	154
Sherm Rabegh[b]	22°44′	4.0	2.7	156	160	11.0	6.1	124	142
	38°58′	4.0	1.4	162	163	2.0	2.5	165	164
Siq[a]	12°40′	35.0	33.0	338	346	23.0	27.0	139	140
	54°04′	17.0	17.3	339	349	13.0	11.4	156	164
Suez[b]	29°56′	4.5	3.3	158	162	56.0	26.0	278	300
	32°33′	1.3	0.8	170	152	14.0	8.7	306	319
Tor[b]	28°14′	4.0	2.6	164	157	8.0	3.2	205	213
	33°37′	2.0	0.8	159	152	1.0	1.6	230	211
Zafarana[b]	29°07′	3.0	3.3	165	163	42.0	21.0	280	300
	32°40′	1.0	0.9	199	152	12.7	6.9	301	320

[a]Stations located in the Gulf of Aden and Indian Ocean.
[b]Stations located in the Red Sea.
[c]Stations located in the Bab el Mandab Strait.

amplitudes near Port Sudan and Jeddah resulting from the presence of the anticlockwise amphidromic system, and the M_2 amphidrome in the Bab el Mandab Strait (Defant, 1961).

A measure of the agreement between the modeled and observed elevations is achieved by examining correlation coefficients between computed and measured amplitudes and phases. Table 2 lists these coefficients together with the number of stations used in the comparison and the respective standard deviations of the differences between the modeled and observed values. In addition, the parameter H is presented, which is an average difference between the observations and model solution and measures overall model performance. This parameter is estimated from the following expression (Davies et al., 1997):

$$H = \frac{1}{N}\sum_{k=1}^{N}[(A_{\text{obs}}\cos g_{\text{obs}} - A_{\text{com}}\cos g_{\text{com}})^2$$
$$+ (A_{\text{obs}}\sin g_{\text{obs}} - A_{\text{com}}\sin g_{\text{com}})^2]^{1/2}, \qquad (4)$$

Table 2
Correlation coefficients (Corr) and standard deviations (SD) between the computed and measured tidal amplitudes and phases

Tidal constituent	N	Amplitude		Phase		H (cm)
		Corr	SD(cm)	Corr	SD(deg)	
Q_1	10	0.97	0.4	0.90	11	0.53
O_1	33	0.99	0.8	0.99	16	1.15
P_1	17	0.99	0.6	0.98	22	0.93
K_1	33	0.99	2.4	0.86	17	2.45
N_2	23	0.73	3.2	0.85	42	4.49
M_2	33	0.83	9.3	0.85	39	9.39
S_2	33	0.94	2.5	0.79	18	2.99
K_2	20	0.91	1.1	0.75	28	1.68

N is the number of the stations; H is an average difference between the observations and computed solution.

where N is the number of the water level stations, A and g are amplitudes and phases, respectively, and suffixes "com" and "obs" denote the computed and observed harmonic constants, respectively.

High correlation coefficients (greater than 0.96 for the amplitudes and 0.85 or higher for the phases) coupled with the small H values (less than 2.5 cm) and low standard deviations (less than 2.5 cm for amplitudes and 23° for phases) indicate accurate replication of the diurnal components by the model. For the major semidiurnal constituents, the model computations do not compare as favorably to the observations as shown by the lower correlation coefficients (less than 0.95 for amplitudes and below 0.85 for phases) and higher values of H ($\sim$3 cm or more for the S_2, N_2, and M_2 components). Note (Table 1 and Fig. 3) that the larger errors of the semidiurnal elevation are not uniformly distributed within the model domain.

Fig. 3 shows mean absolute amplitude and phase differences computed separately for the stations located in the Red Sea (17 stations), Bab el Mandab Strait (six stations) and Gulf of Aden/Indian Ocean (10 stations). Comparison of the measured data to the model solution (Table 1) indicate that in the Gulf of Aden and southern part of the Bab el Mandab Strait, the agreement between the observations and the model is very satisfactory for both diurnal and semidiurnal components. The same conclusion can be reached for the Gulf Aden/Indian Ocean stations displayed in Fig. 3 by examining the means, which are small for both amplitude (less than 2 cm) and phase (less than 7°). This good agreement suggests that the
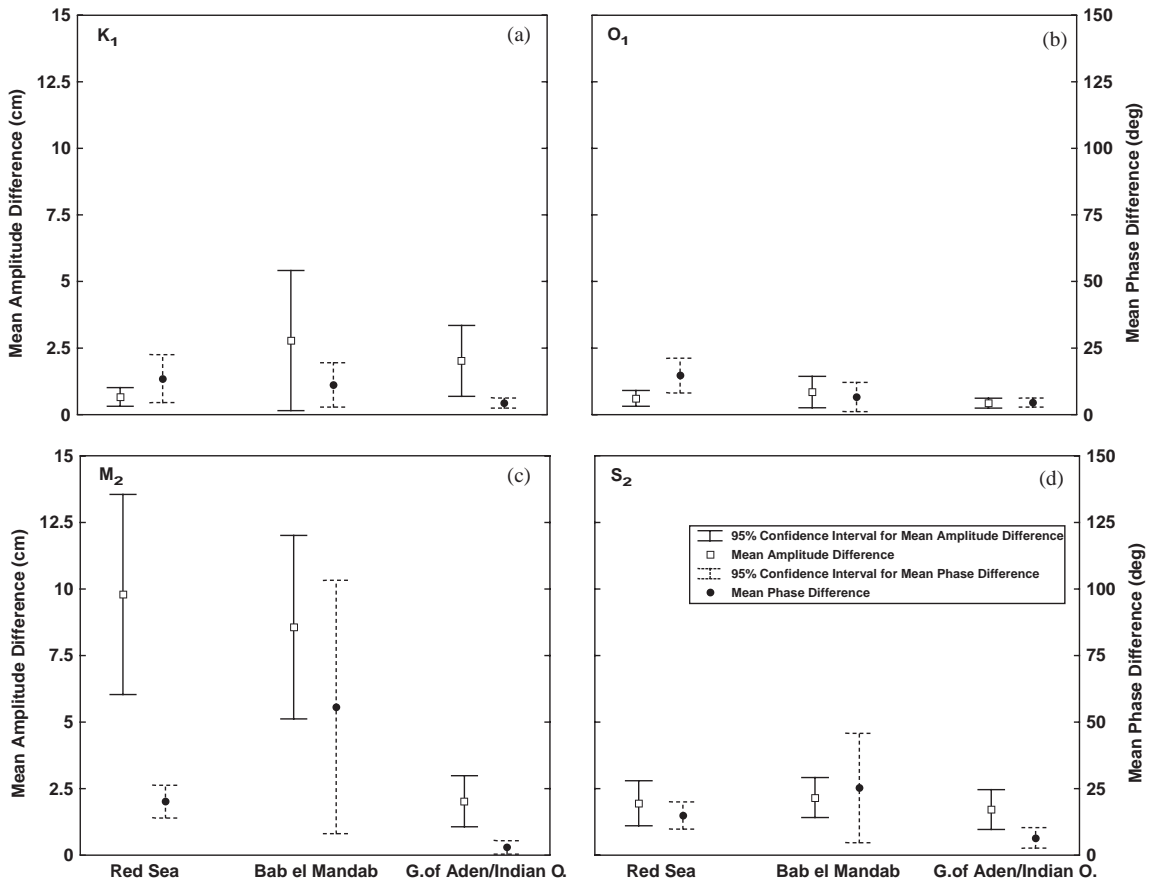

Fig. 3. Mean absolute amplitude and phase differences between the observations and modeled solution and their 95% confidence intervals.

tidal elevation constants taken from the World Ocean Tide Model (Le Provost et al., 1994) represent well the tidal wave incoming from the Indian Ocean. Therefore, the open ocean boundary forcing is not likely to be a major source of the errors observed north of Perim Narrows where the semidiurnal waves are not well simulated, especially with regard to their phases. The largest phase discrepancies are found in the Strait near the amphidrome for the M_2 (Assab, G108 and Mocha) where the difference between the computed and observed phases can be as large as $140°$.

A set of experiments, in which alternate bathymetric values were assigned at the nodes within the Strait, indicates that the phase errors are partly related to the bathymetry. A 10 m decrease of depth in the deep channel and a 5 m decrease of depth in the shoals (at mesh nodes with depths of 7 m or more) between Perim Narrows and Assab-Mocha line resulted in a 15% increase of the M_2 phase, reducing the phase error and causing small changes in the K_1 phase. An increase of the bottom friction coefficient (C_d) to values of 0.05 or larger for the original bathymetric configuration had similar effects on the M_2 phase error, i.e. a reduction. Additionally, it was shown by Grenier et al. (1995) that in regions with strong rectilinear currents, the standard quadratic formulation for the friction term might not be sufficient to properly describe damping of the tidal waves. Since the tidal currents in the Strait are quite strong and very rectilinear, the quadratic bottom friction formulation could be introducing an additional error into the computations. This error, however, is likely small in comparison to errors associated with other forms of tidal dissipation such as form drag, turbulence, internal tide generation, and interaction with nontidal currents, which are not represented in the two-dimensional barotropic model.

Locations (see Fig. 1 and Table 3 for the mooring locations) with observational estimates (5) of the barotropic tidal currents are limited to the Bab el Mandab Strait. In Table 3, the observed and calculated K_1, O_1, M_2, and S_2 tidal currents are described by the parameters of the tidal ellipse (Pugh, 1987). In general, the agreement between computed and measured tidal currents in the Strait is good for both semidiurnal and diurnal constituents. The largest error for the semimajor axis is found for the M_2 at Perim Narrows (moorings A2b, AA1, and AA2b) where the computed amplitudes are, on average, 20% smaller than the measured ones. For other constituents at Perim Narrows as well as for all tidal components at C mooring and the Hanish Sill (mooring B2b) the difference between computed and observed semimajor axes is always less than 20% of those estimated solely from the observations. The modeled semiminor axes are very small (2 cm/s or less) and comparable with those computed from the observations. The difference between the model and observed inclinations is, on average, 4% of the observed inclination angles (measured counterclockwise from east), while the phase difference is always smaller than 1 h for all considered constituents. Additionally, the H values computed separately for along and cross-strait velocity components are listed in Table 4. The H values, except the M_2 component, are small (<2.30 cm/s), indicating that in the Strait, the barotropic tidal currents are well simulated by the model.

4. Tidal elevations and currents in the Strait

Fig. 4 displays computed coamplitudes (in cm) and cophases (in degrees, GMT) of the tidal elevations for the K_1, O_1, M_2, S_2, N_2, and K_2 constituents. Similar to findings from data analyses (Vercelli, 1925, 1927; Siedler, 1969; Jarosz, 2002), K_1 (O_1, P_1 and Q_1 amplitudes are, on average, 50%, 31%, and 9%, respectively, of the K_1) and M_2 (amplitudes of the S_2, N_2 and K_2 are, on average, 45%, 48%, and 9%, respectively, of the M_2) are the dominant constituents in the Strait. Furthermore, the amplitudes of all tidal components show very similar behavior in the Strait, i.e. little variability in the cross-strait direction and rapid attenuation of the amplitudes in the along-strait direction. The largest values are found near Perim Narrows and the smallest ones are present at the northern end of the Strait. The amplitude and phase distributions indicate that the M_2 and S_2 waves have amphidromic systems

Table 3

Comparison between observed (Obs) and computed (Com) tidal current ellipse parameters: semimajor axis (M), semiminor axis (Mn), inclination angle (θ, measured counterclockwise from east), and phase (g, GMT)

Mooring	Latitude(N)/Longitude(E)	Ellipse Parameters	K_1		O_1		M_2		S_2	
			Obs	Com	Obs	Com	Obs	Com	Obs	Com
A2b	12°45.12′	M (cm/s)	29.7	29.4	16.4	17.3	29.2	25.0	10.2	9.1
	43°16.89′	Mn(cm/s)[a]	−1.5	−1.4	−0.5	−1.0	−1.0	−0.7	−0.3	−0.2
		θ (°)	91.3	98.8	92.5	97.9	94.3	99.0	94.3	99.1
		g (°)	68.3	73.2	68.5	74.7	200.8	221.0	227.0	246.0
AA1	12°43.26′	M (cm/s)	31.9	30.0	18.7	17.4	32.5	24.6	11.2	9.5
	43°14.61′	Mn(cm/s)[a]	−0.9	−1.7	−0.1	−1.0	−0.9	−0.7	−0.6	−0.2
		θ (°)	104.4	104.6	104.3	104.6	105.4	104.6	105.2	104.3
		g (°)	88.6	72.1	89.2	75.0	234.0	222.3	258.5	246.5
AA2b	12°43.64′	M (cm/s)	29.0	28.9	16.7	16.1	29.6	23.9	9.3	8.8
	43°16.60′	Mn(cm/s)[a]	−0.7	−2.0	−0.3	−0.9	−0.5	−0.4	−0.2	−0.1
		θ (°)	94.6	95.0	94.2	94.3	96.9	96.6	96.9	96.0
		g (°)	71.3	72.1	74.6	73.9	200.8	220.0	223.4	246.0
C	13°20.48′	M (cm/s)	13.8	15.1	7.2	8.6	16.2	13.4	6.2	5.5
	42°54.22′	Mn(cm/s)[a]	1.2	0.6	0.6	0.4	0.2	0.3	0.2	0.1
		θ (°)	133.5	132.8	132.0	133.3	128.3	132.7	124.7	132.0
		g (°)	73.4	74.6	74.4	76.6	220.9	222.9	248.1	248.9
B2b	13°42.62′	M (cm/s)	15.6	16.5	9.4	9.1	15.0	15.0	6.0	6.4
	42°32.35′	Mn(cm/s)[a]	−0.6	−0.4	−0.4	−0.3	−0.3	−0.3	−0.1	−0.1
		θ (°)	133.0	122.0	134.2	123.0	133.9	123.0	133.4	123.8
		g (°)	73.9	78.3	77.6	81.8	204.6	223.0	230.3	250.0

[a] A sign of the semiminor axis (Mn) indicates a sense of tidal current rotation, which is clockwise for the positive values and counterclockwise for the negative values.

Table 4

Average difference (H) between the observed and computed cross- and along-Strait velocity components

	Q_1	O_1	P_1	K_1	N_2	M_2	S_2	K_2
Cross-Strait Velocity (cm/s)	0.21	0.75	0.57	1.35	0.46	1.49	0.76	0.46
Along-Strait Velocity (cm/s)	0.20	1.32	1.24	2.22	1.81	5.27	1.31	0.83

located near the northern end of the Strait as shown in Figs. 4c and d. Vercelli (1925) and Defant (1961), based on the limited data, postulated that, in the Strait, there is an amphidromic point of the M_2 tide, and this amphidrome is located near Assab southwest of that suggested by the model results. The spatial distribution of the N_2 amplitude and phase near the Hanish Islands resembles that of a degenerate amphidromic system (Fig. 4e), while the K_2 phase (Fig. 4f)

decreases from less than 150° near Perim Narrows to 30° just north of the Hanish Islands. The phase of the diurnal constituents vary little in the major part of the Strait, and the model results imply that all diurnal constituents have anticlockwise amphidromic systems located north of the Bab el Mandab Strait (K_1 and P_1 at ~15°N; O_1 and Q_1 at ~14° 25′N).

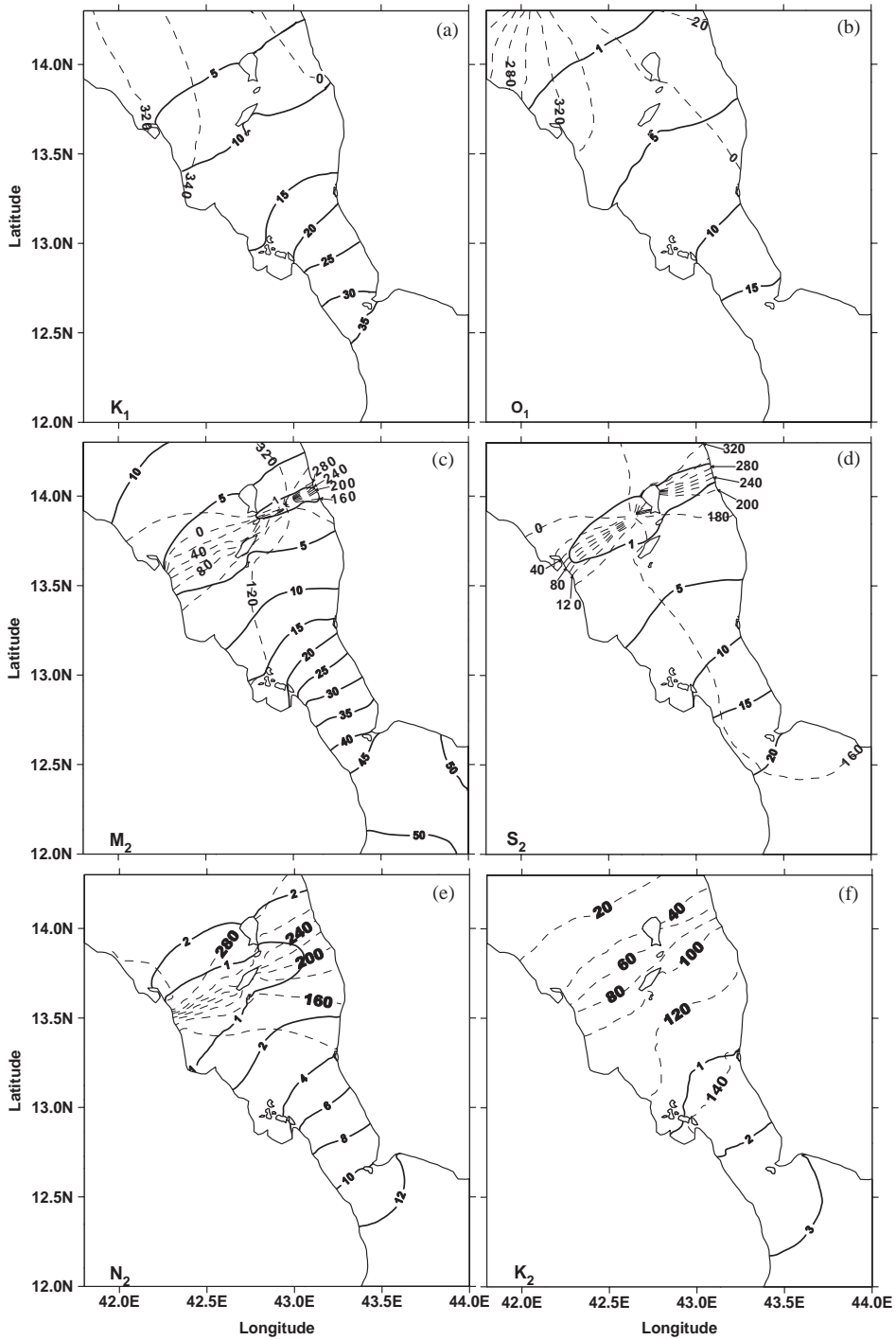The amplitudes and inclination of the semimajor axis for four principle constituents, K_1, O_1, M_2,

Fig. 4. Model coamplitudes (in cm; solid line) and cophases (deg, GMT; dashed line) for the (a) K_1, (b) O_1, (c) M_2, (d) S_2, (e) N_2, and (f) K_2 constituents.

and S_2 are displayed in Fig. 5 (inclination arrows are shown at a subsampled number of the model nodes for clarity). For all eight tidal components, distributions of the semimajor axis amplitudes show amplification of tidal currents as they flow into the Bab el Mandab Strait from the Gulf of Aden. The strongest currents are generated by the K_1 (semimajor axis amplitudes of the O_1, P_1, and Q_1 are, on average, 55%, 38%, and 10%,

respectively, of those associated with the K_1) and M_2 (semimajor axis amplitudes of the S_2, N_2, and K_2 are, on average, 41%, 25%, and 5%, respectively, of those associated with the M_2). Furthermore, the amplitudes of the K_1 and M_2 currents are comparable. The most energetic flow is present in the narrowest part of the Strait (between Perim Narrows and Assab-Mocha line) with the maximum modeled amplitudes found near the Perim
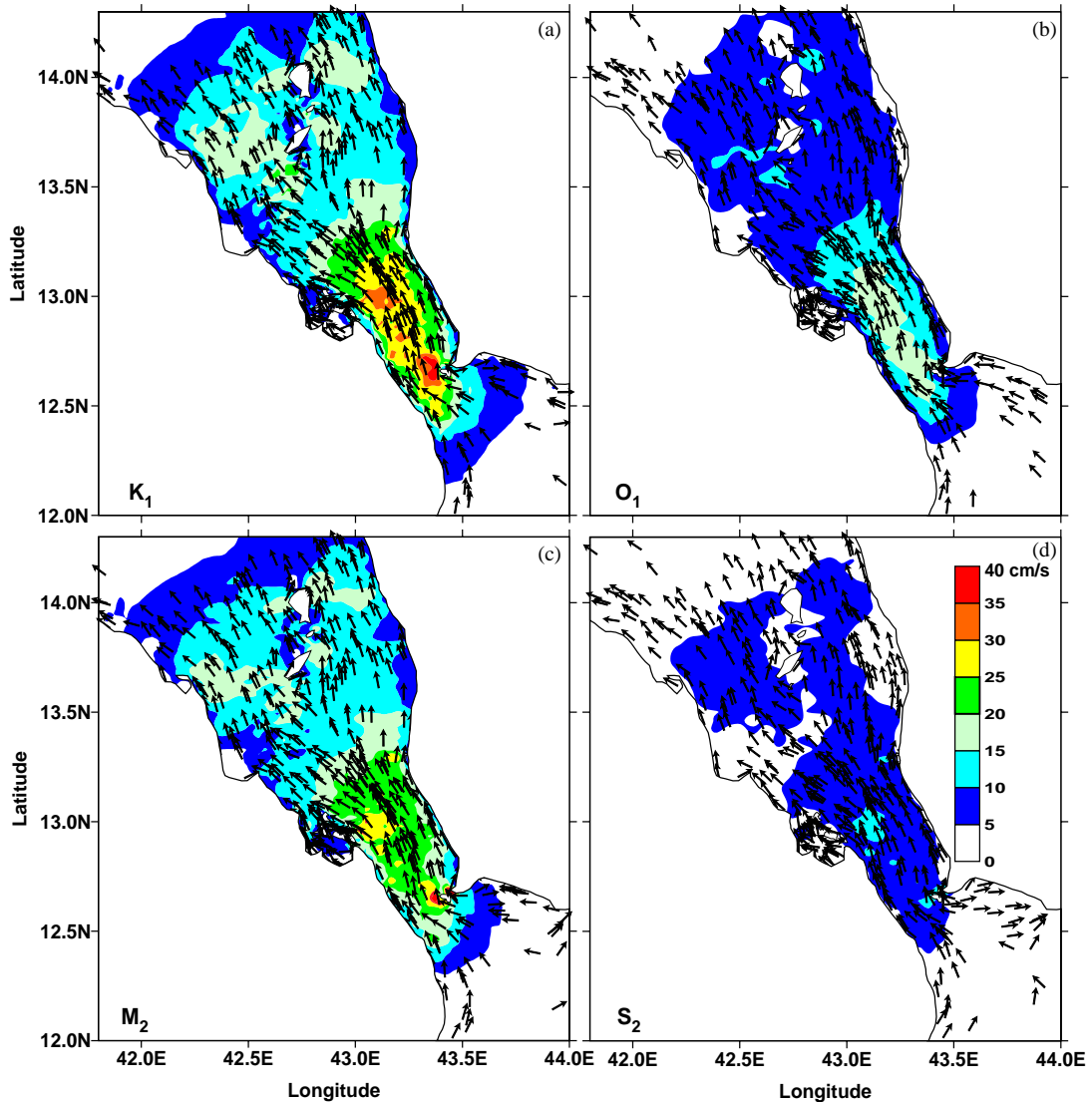
Fig. 5. Model amplitudes (cm/s; a color scale) and direction (arrows) of the current semimajor axis for the (a) K_1, (b) O_1, (c) M_2, and (d) S_2 constituents.

Island where, for instance, the speeds of the K_1 and M_2 currents may reach 40 cm/s. Farther north, the current amplitudes associated with a single constituent rarely exceed 20 cm/s. For all constituents, the direction of the maximum flow is generally aligned with the along-strait direction. Similar to the results obtained from the observational analysis of Jarosz (2002), the tidal currents are nearly rectilinear in the Strait (amplitudes of the semiminor axis are always smaller then those of the semimajor one and they are not larger than 5 cm/s). The phase distributions (not shown) indicate

that for the same constituent, the currents turn earlier in the shallow waters than those observed in the deeper parts of the Strait. In addition, the phase difference between maximum tidal velocity and elevation is approximately 90° in the central part of the Bab el Mandab Strait (depths below 60 m) for all considered constituents.

The next two figures (Figs. 6 and 7) display, as an example, the modeled tidal elevations and currents observed during spring tides in the Strait. Fortnightly variations in this Strait are generated not only by interactions between the M_2 and S_2
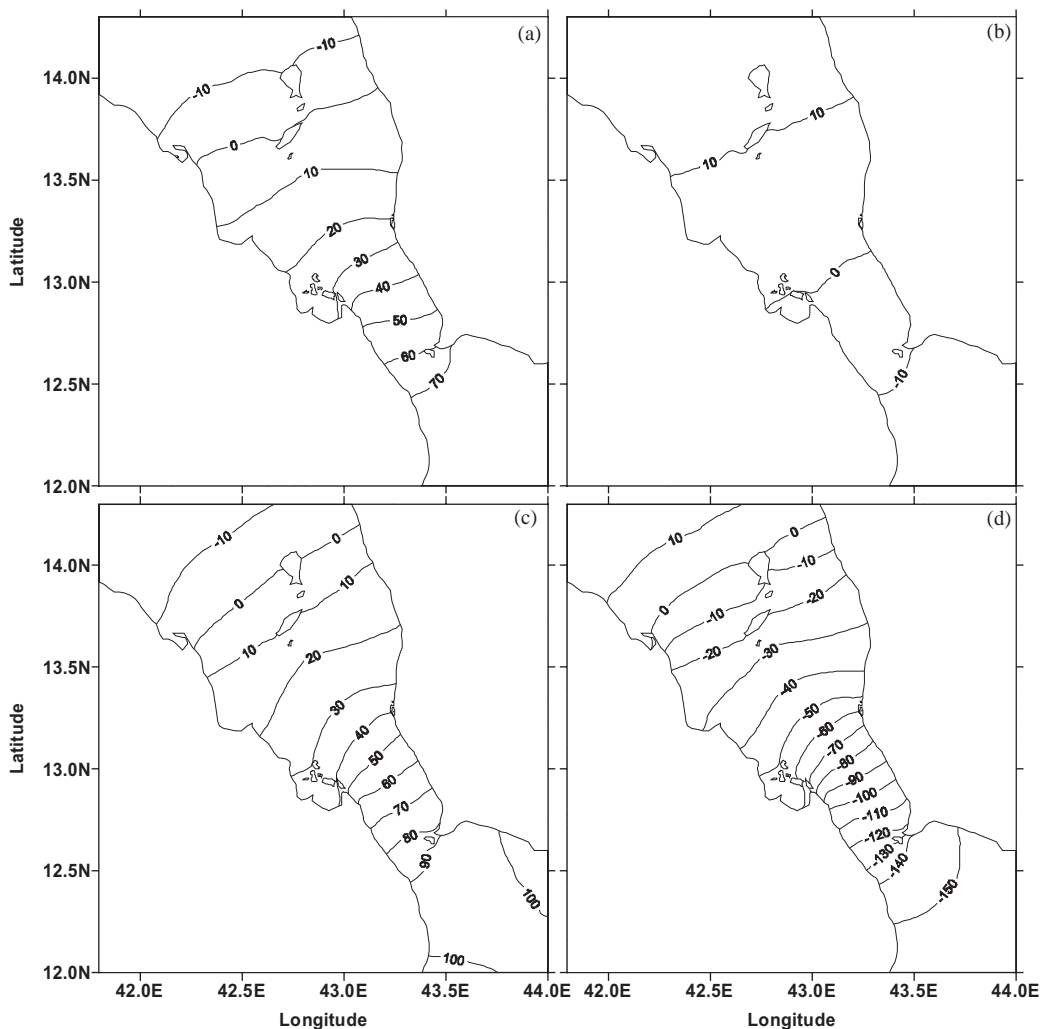
Fig. 6. Distribution of the spring tide water elevation (in cm) in the Bal el Mandab Strait at time of (a) lower high water (LHW), (b) higher low water (HLW), (c) higher high water (HHW), and (d) lower low water (LLW) at Perim Narrows.
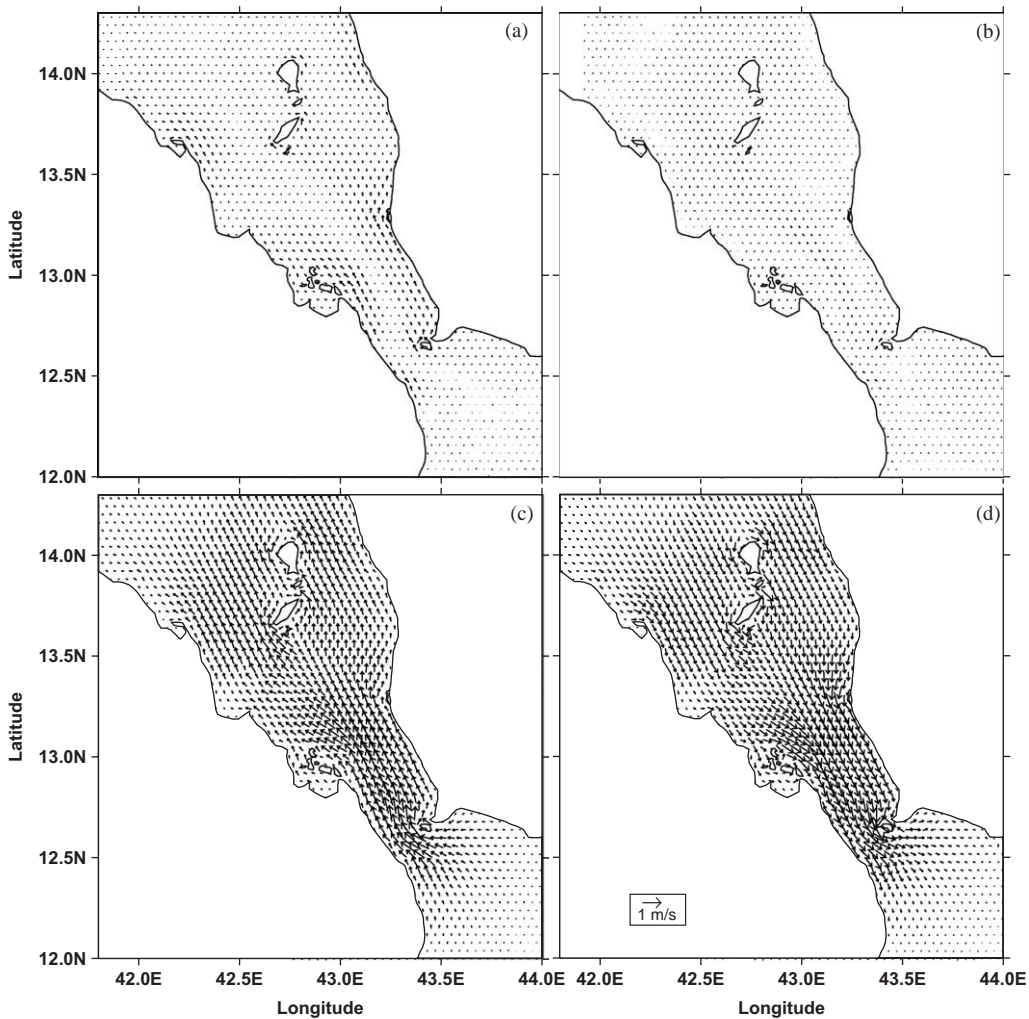
Fig. 7. Spring tide currents in the Bab el Mandab Strait (a) ∼4 h after LHW, (b) ∼3 h after HLW, (c) ∼3 h after HHW, and (d) ∼4 h after LLW at Perim Narrows.

components, but also by interactions between the K_1 and O_1 constituents; for convenience of this discussion, we refer to the largest tides generated by all considered constituents in the fortnightly cycle as spring tides as opposed to the lowest tides that we refer to as neap tides. For all displayed plots the times of the high or low waters are referenced to those observed at Perim Narrows.

The spring tides in this Strait are characterized by two high and two low waters. Two nearly equal high and low water stages are mainly observed near the Hanish Islands where the tidal elevation

fluctuations are dominated by the semidiurnal tides. South of the islands, these maxima and minima are more and more dissimilar due to the changing character of the tides from semidiurnal to mixed. The distributions of the tidal elevation for both high water stages of the spring tides (Figs. 6a and c) are fairly similar. They both show the largest elevations in the southern part of the Strait with magnitudes of ∼70 and ∼90 cm near Perim Narrows for lower high water (LHW) and higher high water (HHW), respectively. Furthermore, the large elevation gradients are present in the along-

strait direction while simultaneously showing little or no variability in the cross-strait direction. Similar to the high water stages, the low water elevation distributions show little variability in the cross-strait direction and large variations in the along-strait direction; largest elevation gradients are present during lower low water (LLW) and much smaller ones occur at higher low water (HLW). Furthermore, when LLW is observed at Perim Narrows (Fig. 6d), the low water (negative values) is generally present throughout the entire Strait, while for the HLW stage (Fig. 6b), only the part of the Strait between Perim Narrows and the Assab-Mocha line is actually in the low water stage. Farther north, the tidal elevation distribution implies rather high water stage.

The currents are in the flood stage about 4 h after LHW at Perim (Fig. 7a). The direction of the flow shows some variability, but in general, the barotropic currents flow into the Strait with the speeds rarely exceeding 20 cm/s. Fig. 7b displays the speed and direction approximately 3 h after HLW at Perim Narrows. Similar to the previous stage, the speeds are weak and rarely reach 15 cm/s. The flow direction varies greatly and the well-defined outflow (speed between 10 and 15 cm/s) is generally confined to the deep channel. About 3 h after HHW, the tidal currents are at the maximum flood stage (Fig. 7c). The flow is very energetic in the entire Strait with the maximum velocity reaching above 100 cm/s at Perim Narrows. The direction of the flood flow is nearly uniform showing the well-defined inflow across the entire Strait. Finally, about 4 h after LLW at Perim Narrows (Fig. 7d), the currents are at the maximum outflow. The direction of the flow varies very little and the outflow is observed across the entire Strait with the speeds comparable to those of the maximum flood currents.

During 24 h of neap tides, one may see one low and one high water or, similar to the spring tides, two high and two low waters (data not shown). The general features of the elevation distribution, such as higher magnitudes near Perim Narrows, large gradients in the along-strait direction, little variability in the cross-shore direction, are identical to those observed during the high and low water of the spring tides. The only difference, as

expected, is a magnitude of the tidal elevations, which is lower in the Strait for the neap tides. During these tides, the maximum speeds of the flood/ebb flow associated with HHW/LLW are generally between 25 and 35 cm/s south of the Assab-Mocha line. Farther north, they do not exceed 20 cm/s. Similar to the HHW flood or LLW ebb of the spring tides, there is little variability in the direction of these tidal flows, which generally show inflow and outflow, respectively, across the entire Strait. If the second flood and ebb are observed, the currents are even weaker, and their direction is quite variable.

5. Tidal residual circulation in the Strait

Due to variable bathymetry, the tidal flow may generate residual currents through nonlinear interactions (Zimmerman, 1978). These tidal residual currents often play an important role in the local mean circulation, and in the case of the Bab el Mandab Strait, they may also contribute to the transport of the Red Sea waters to the Gulf of Aden/Indian Ocean system.

To extract the time-averaged residual motion, which is induced by the eight primary tidal constituents (K_1, O_1, P_1, Q_1, M_2, S_2, N_2, and K_2) in the Strait, the computed currents were averaged over a 29-day period (Kowalik and Polyakov, 1998), and the results of this averaging are shown in Fig. 8. In general, the residuals are weak with an average speed below 1 cm/s. In the deep channel, to which the Red Sea water outflow is confined (Murray and Johns, 1997), the residual current speeds are even lower and do not exceed 0.5 cm/s. At the Perim transect (see Fig. 1 for its location), for instance, the transport generated by the residual flow in the deep channel (depths of 50 m or more) is directed towards the Gulf of Aden but it is very small ($\sim 3.45 \times 10^{-3}$ Sv, $1 Sv = 10^6 m^3/s$) when compared with the volume transport of 0.37 Sv associated with the mean circulation (Murray and Johns, 1997). The strongest residual flow is generally found near the islands and in the shallow parts of the Strait located between Perim Narrows and Assab-Mocha line. Near Perim or the Hanish Islands, for instance, the speed of the
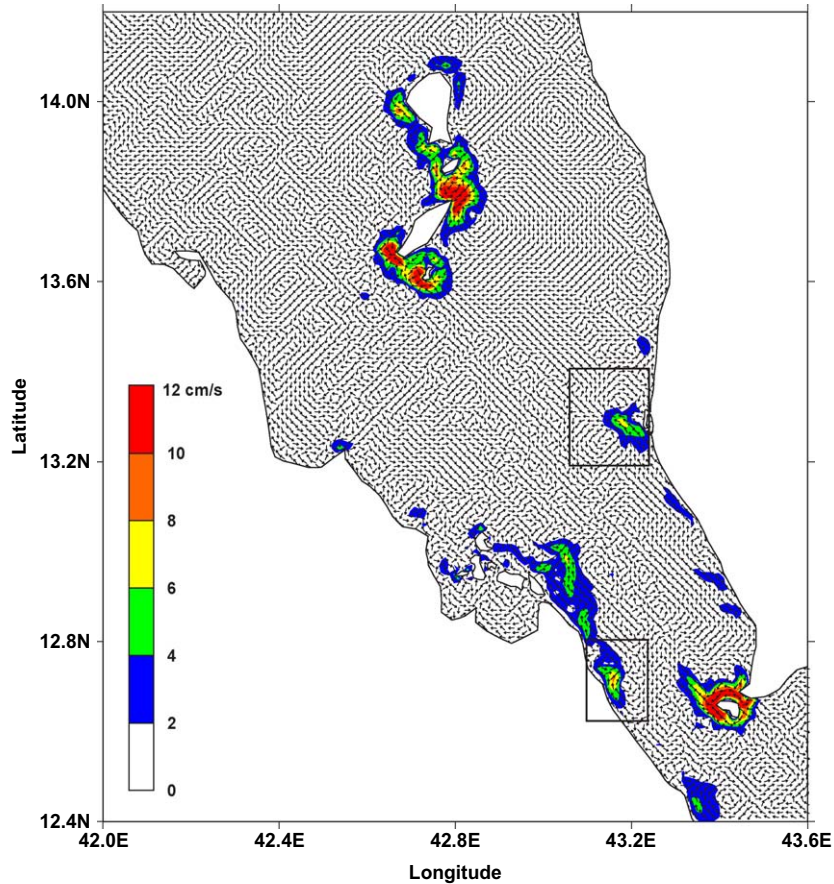
Fig. 8. Time-averaged residual tidal flow in the Bab el Mandab Strait (a color scale—speeds in cm/s; arrows—direction).

residual currents can be as high as 20 cm/s. These high speeds observed near the islands and headlands may be partly generated by sharp changes in the coastline associated with the model grid despite its high resolution. The time-averaged residual flow also displays several small clockwise and counterclockwise eddies such as those located west of Mocha or south–east of Ras Dehaneba (see circulation patterns inside the black rectangles in Fig. 8). A lack of high resolution in situ observations in these areas prohibits verification of the existence of these eddies.

In addition to the time-averaged residual currents, the time-dependent residual flow was also analyzed. These residuals were extracted from the model computed time series by removing motions with periods less than 2 days. The

amplitudes of these currents (not shown) are slightly lower than those of the time-averaged flow with the maximum amplitudes being below 15 cm/s. Similar to the time-averaged residual flow, the most energetic currents are again observed near the Perim and Hanish Islands. Additionally, small eddies are present in the time-dependent flow, and these eddies are better developed during the spring tides. These time-dependent fluctuations are dominated by a fortnightly cycle. Spectral analysis indicates that most of the energy at low frequencies is indeed in the fortnightly frequency and some in the monthly frequency. None of the low frequency constituents is included in the forcing. Thus, in this region, they arise through interactions between those constituents, which are used to force the model. The results indicate that
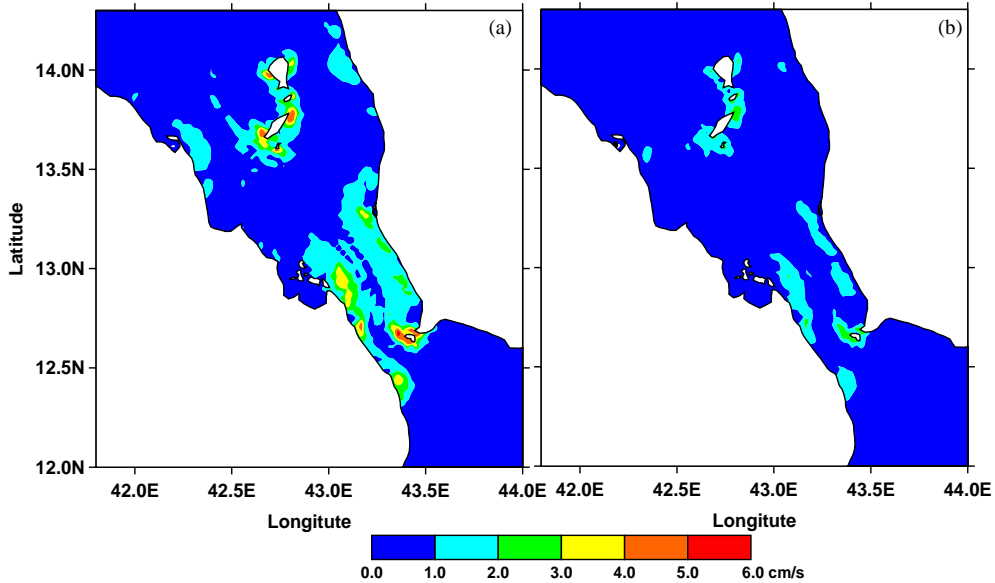
Fig. 9. Amplitudes (in cm) of the semimajor axes of (a) the fluctuations generated by the K_1 and O_1 interactions and (b) the M_{sf} constituent.

among these long period tidal constituents, the M_{sf} (M_2 and S_2 interactions) and tide having a 13.66-day period (generated by K_1 and O_1 nonlinear interactions) are dominant components in the Strait. Such K_1 and O_1 interactions have been also observed in other ocean regions as described by Brink (1995) and Kowalik and Polyakov (1998). Fig. 9 shows the spatial structure of the semimajor axes of the M_{sf} and 13.66-day components as obtained from the harmonic analyses of a 1-year-long model time series. The amplitudes of this axis vary between 0.01 and 5.30 cm/s for the M_{sf} and between 0.01 and 5.48 cm/s for the 13.66-day component. Additionally, the amplitudes of the M_{sf} constituent in the Strait are generally smaller than those associated with the oscillations generated by the K_1 and O_1 tidal components.

6. Barotropic energy flux and dissipation

The energy flux (Kowalik and Proshutinsky, 1993; Foreman et al., 1995) is given by

$$\vec{F} = (h + \xi)\rho_0(0.5\left|\vec{U}\right|^2 + g\xi)\vec{U}, \qquad (5)$$

where h is the water depth, ξ is the tidal elevation, ρ_0 is representative seawater density ($= 1026$ kg/ m^3), $\vec{U}$ is the current velocity vector, and g is the acceleration due to gravity. This energy flux includes the contribution of both kinetic and potential energy. In the Bab el Mandab Strait, the flux of the kinetic energy is always smaller than that for the potential energy, on average, by four orders of magnitude. For example, the flux of the K_1 kinetic energy is, on average, 7×10^{-2} W/m while the average flux of the K_1 potential energy is 13.9×10^2 W/m. The same fluxes for M_2 are 5×10^{-2} and 8.5×10^2 W/m, respectively.

The average energy fluxes over a tidal period for the K_1 and M_2 constituents are shown in Fig. 10. For each constituent, the average energy flux was computed by averaging the flux time series obtained from Eq. (5) over the constituent period. Additionally, the elevations and currents, required for the flux time series computations, were generated using the model harmonic constants and a time interval of 1 min. It is very apparent that the average fluxes associated with two dominant tidal components display different behavior in the Strait. The K_1 constituent has generally one source of energy (Fig. 10a), which is
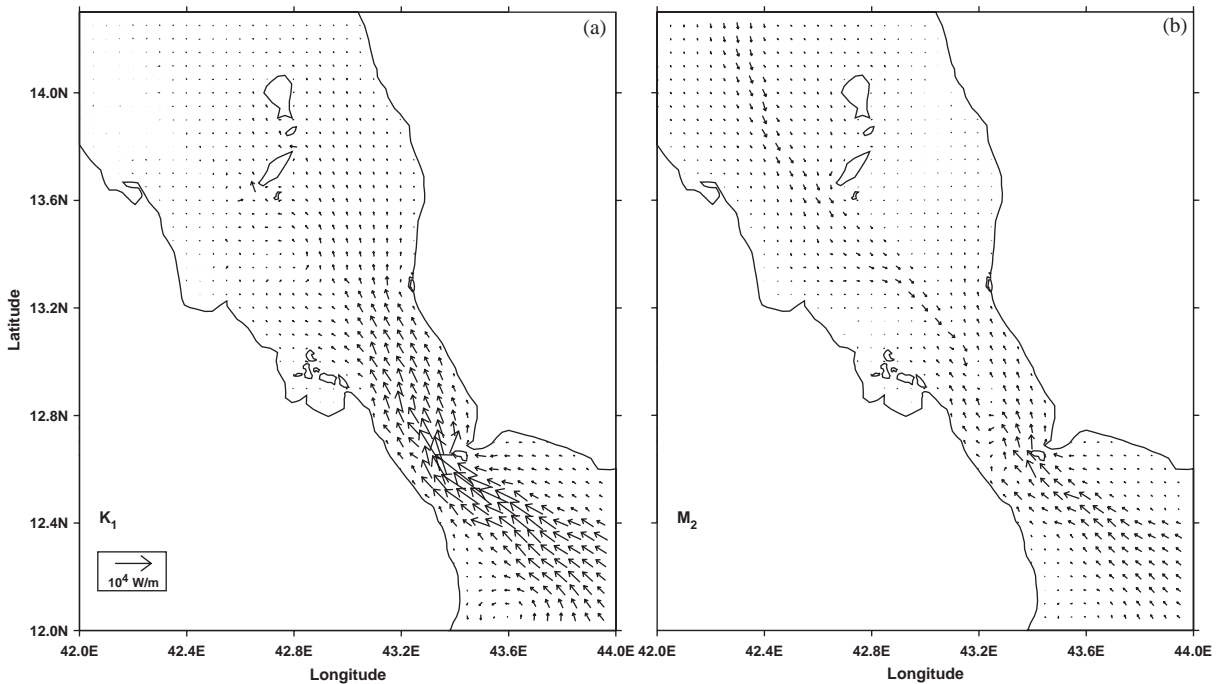
Fig. 10. Mean tidal energy flux per unit length (in W/m) for the (a) K_1 and (b) M_2 constituents.

the advective flux from the Gulf of Aden into the Strait. The additional contribution of the K_1 energy from the Red Sea proper is negligible because the fluxes associated with this source are at least two orders of magnitude smaller than those from the Gulf. Similar to the K_1, other diurnal constituents also have one major source of energy, which is flux from the Gulf of Aden. In contrast, there are two comparable sources of energy for the M_2 constituent (Fig. 10b): one is the flux directed from the Gulf of Aden and another is the flux from the Red Sea proper. The S_2 and K_2 have two fairly comparable energy sources as that for the M_2. For the N_2, however, the computed fluxes from the Red Sea are, on average, one order of magnitude smaller than those from the Gulf. Additionally, Fig. 11 shows the average energy fluxes for the spring and neap tides (both spring and neap fluxes are 25-h averages). These spring and neap fluxes, which give estimates for a maximum and a minimum of the barotropic tidal fluxes in the Strait as generated by eight principle constituents, clearly indicate that the major flux of

the tidal energy into the Strait is again from the Gulf of Aden.

Table 5 lists tidal power fluxes normal to two transects that are located near Perim Narrows and the Hanish Sill (see Fig. 1 for their locations). All estimates are the net fluxes through the transects with the flux into the Strait being positively defined and the flux out of the Strait being negatively defined. In addition to the constituent fluxes, Table 5 lists fluxes of the spring and neap tides (spring/neap). The spring and neap values are the averages calculated over 25 h periods beginning at 00:00 GMT on June 12, 1995 and ending at 00:00 on June 20, 1995, respectively, including all eight constituents.

The values listed in Table 5 indicate that regardless of the constituent or spring/neap tide, energy is generally advected to the Strait. The outgoing fluxes (see, for instance, diurnal component and neap fluxes) are observed only along the Hanish transect and their values are just a small fraction of those transmitted through the Perim transect. In general, the majority of the barotropic
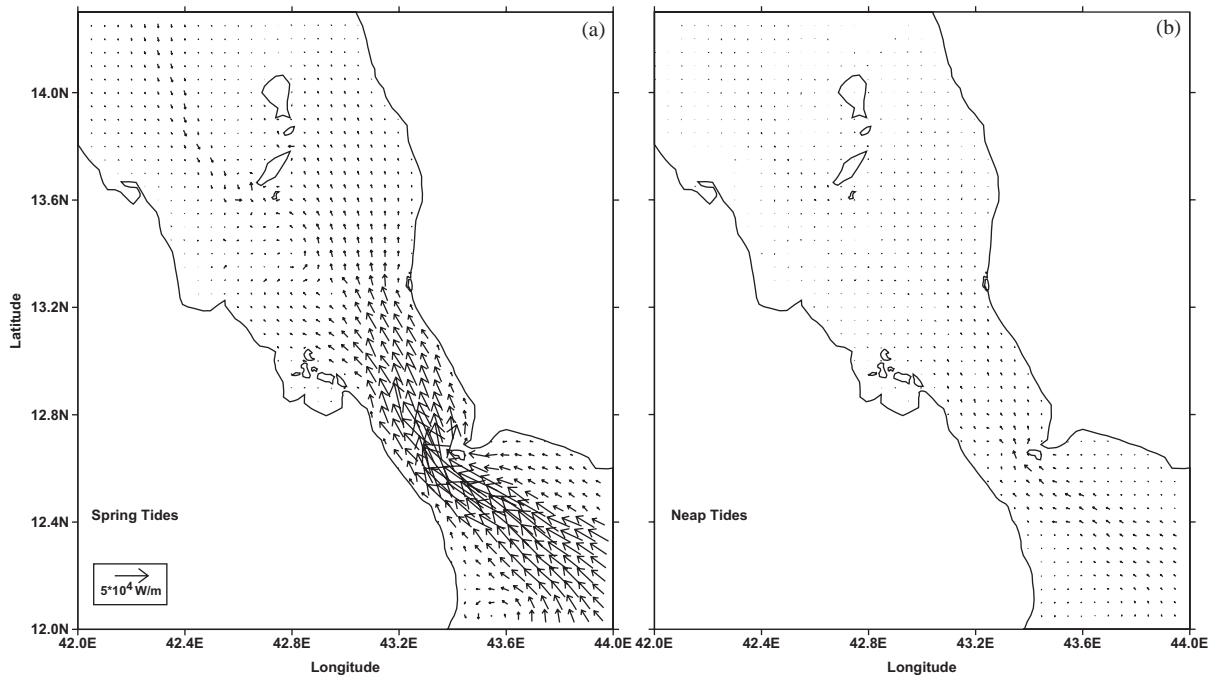
Fig. 11. Mean tidal energy fluxes (25-h averages; in W/m) for (a) spring and (b) neap tides.

Table 5
Net power flux (in Gigawatts) normal to the transects shown in Fig. 1

Transect	K_1	O_1	P_1	Q_1	M_2	S_2	N_2	K_2	Spring	Neap
Perim (1)	0.248	0.091	0.032	0.004	0.111	0.032	0.017	0.001	1.472	0.288
Hanish (2)	−0.022	−0.007	−0.002	−0.0003	0.091	0.005	−0.002	0.001	0.128	−0.003

tidal energy is advected to the Bab el Mandab Strait from the Gulf of Aden where both diurnal and semidiurnal tides are strong. Since the tides in the Red Sea are weaker than those of the Gulf of Aden and semidiurnal in nature it is not unexpected that the contribution of energy from this Sea would be small, especially for the diurnal components. The net energy fluxes along the Hanish transect are indeed small with the exception of those associated with the M_2 and K_2 constituents, which are comparable with the energy input from the Gulf as reflected at the Perim Narrows transect (Table 5). In addition, the model simulation with the equilibrium tidal potential excluded from the computations shows

that the K_2 energy flux from the Red Sea to the Strait is zero at the Hanish transect, while that of the M_2 flux is extremely small and equal to 1.9039×10^{-5} GW at the same location. These findings imply that the M_2 and K_2 energy fluxes across the Hanish transect are directly generated in the Red Sea by the equilibrium tides.

Due to the small outflowing fluxes, almost all tidal energy is dissipated within the Strait. Energy dissipation for all cases is estimated as a net power flux into a polygon encompassed by Perim and Hanish transects and the coastline of the Strait. Note that only one dissipation mechanism, bottom friction, is included in this particular implementation of the ADCIRC model. Lateral and vertical

mixing and energy lost to the generation of internal tides are not included. When the dissipation process is viewed in terms of each constituent, more, on average, semidiurnal energy (M_2—98%, S_2—98%, N_2—85%, and K_2—95%) than diurnal (K_1—90%, O_1—91%, P_1—92%, and Q_1—92%) is lost within the Strait (95% versus 91% of that which enters). A high percentage of dissipation is also observed during the chosen spring tide period (98%). The dissipation during neap tides is slightly lower but still large, equal to 96%. Within the polygon encompassed by the chosen transects, the dissipation is estimated as 0.226, 0.084, 0.03, and 0.0037 GW for the diurnal constituents K_1, O_1, P_1, Q_1, and 0.202, 0.037, 0.015, and 0.002 GW for the semidiurnal constituents M_2, S_2, N_2, and K_2. For spring and neap tides, the dissipation is 1.6 and 0.282 GW, respectively.

To investigate further the dissipation of the barotropic tides in the Bab el Mandab Strait, i.e. to identify areas with high tidal energy losses and find differences, if any, in a dissipation pattern among different constituents, a rate of energy dissipation was computed. This rate is defined as (Tsimplis et al., 1995; Munk, 1997):

$$d = \frac{1}{T} \int_0^T C_d \rho_0 (U^2 + V^2)^{3/2} \, dt, \qquad (6)$$

where C_d is the bottom drag coefficient (= 0.003), ρ_0 is the seawater density (= 1026 kg/m^3), U, V are the velocity components at a given grid point, and T is the tidal period. Fig. 12 displays, as an example, the spatial distribution of this rate due to the K_1, M_2, spring and neap tides. The spatial distributions of the dissipation rate demonstrate that there are similarities in the dissipation pattern of the diurnal and semidiurnal tides. Furthermore, the dissipation processes are not uniform in the Strait. The maximum rate of energy dissipation, for the K_1 and M_2 tides displayed in Figs. 12a and b, is generally found in the narrowest part of the study area located between Perim Narrows and the Assab-Mocha line, i.e. in the region with the maximum tidal velocities. The same pattern holds true for the other tidal constituents considered. In this region of the maximum dissipation, the rate

reaches values of or greater than 0.01 W/m^2 for both K_1 and M_2. Farther north, where the tidal flow is weaker, the dissipation rate is generally on the order of 10^{-3} W/m^2. The dissipation rate estimates for other constituents are at least one order of magnitude smaller than those of the K_1 and M_2. The spatial patterns of the dissipation rate associated with the spring and neap tides (Figs. 12c and d) are very similar to those of the diurnal and semidiurnal constituents, and in case of the neap tides, the absolute values of the dissipation rates are comparable to those of the K_1 and M_2. For the spring tides, however, the dissipation rate estimates are generally one order of magnitude larger than those associated with the K_1, M_2, or neap tides.

7. Summary and conclusions

Recent observations (Jarosz, 2002) indicate that tidal motion is a fundamental, clearly non-negligible, aspect of the flow field in the Bab el Mandab. The available measurements, however, are spatially dispersed and too sparse to examine in detail the tidal dynamics in this Strait. Thus, barotropic tides in the Bab el Mandab Strait are numerically simulated with the high resolution, two-dimensional form of the finite element hydrodynamic model ADCIRC (Luettich et al., 1992; Westerink et al., 1994) to examine (1) variability of the barotropic tidal elevations and currents, (2) residual tidal circulation and its possible contribution to the Red Sea water outflow, and (3) to estimate barotropic energy fluxes and energy dissipation rates. To our knowledge, this model is the first numerical attempt focused on tides in this Strait.

Comparisons with the available observations indicate that the model simulates well the diurnal tidal elevations when compared to the observed values. Furthermore, the comparison between observed and computed tidal currents shows that the tidal currents are also well replicated in the Strait for both semidiurnal and diurnal constituents. The model performance, however, for the semidiurnal elevations is less satisfactory mainly due to the errors between observed and computed
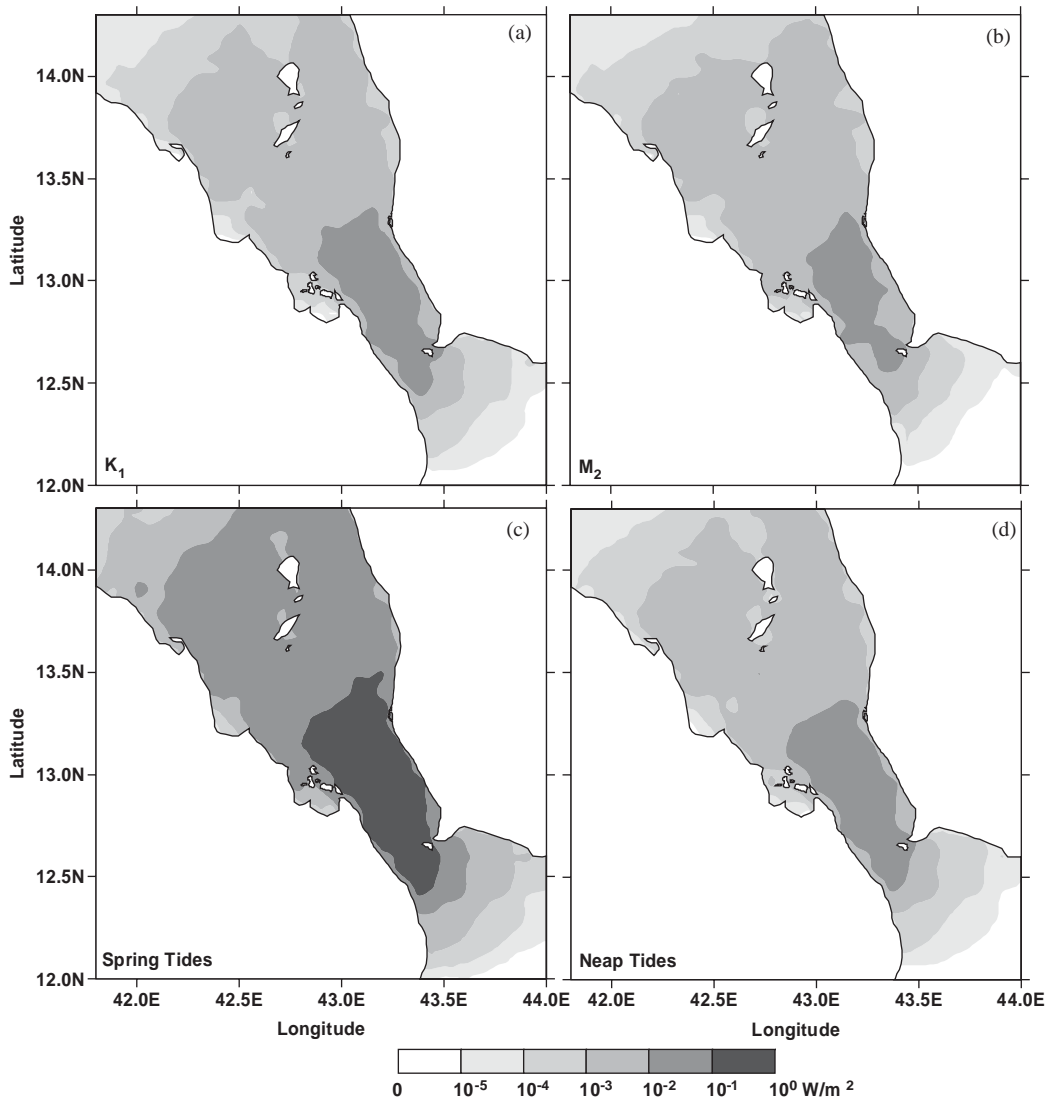
Fig. 12. Tidal energy dissipation rate (W/m^2) for the (a) K_1, (b) M_2, (c) spring, and (d) neap tides.

phases in the region of amphidromic systems for these tides in the Strait. These discrepancies between observed and computed phases are not unexpected in such regions because small errors in the position of the amphidrome usually lead to large phase errors.

The model computations indicate that the tidal elevation range varies between approximately 2 m near Perim Narrows to less than 1 m near the Hanish Islands. The barotropic tidal currents generated by the eight primary constituents have the largest amplitudes between Perim Narrows and Assab-Mocha line where their combined speeds are above 1 m/s. Farther north, the current amplitudes are reduced by approximately 50% of those observed in the narrow southern part of the Strait. The amphidromic points for the M_2, S_2, N_2 in the Strait and the amphidromes for the Q_1, O_1, P_1, K_1, and K_2 constituents just north of the Hanish Islands together with nearly 90° phase

difference between the tidal elevations and currents imply that the tides in the Strait have some characteristics of standing waves.

Residual circulation induced by the barotropic tidal currents is rather weak with the speeds often less than 1 cm/s in the major part of the Strait, and it contributes little to the overall transport of the Red Sea waters to the Gulf of Aden/Indian Ocean system. This residual circulation consists of mean (time-averaged) and fluctuating (deviation from the mean) components. The fluctuating residual flow is dominated by fortnightly oscillations, which are generated by the interactions of the K_1 and O_1 constituents as well as the interaction between the M_2 and S_2 components.

The mean energy fluxes are small mainly due to the approximately $90°$ phase difference between tidal velocity and elevation, which is observed in the major part of the Strait; however, these flux estimates should be very useful for comparison with future calculations of the energy loss by internal tide generation or/and turbulent mixing in the Strait. Our model results show that the diurnal constituents have one major source of energy, the advective flux from the Gulf of Aden. In contrast, two comparable sources of energy are identified for the M_2, and K_2 constituents: one is the advective flux from the Gulf of Aden and another is the flux from the Red Sea proper. The latter fluxes for both tidal components are directly generated in the Red Sea by the equilibrium tides. For the N_2 and S_2, the major flux comes from the Gulf of Aden. Furthermore, very small fluxes from the Strait to the adjacent basins indicate that the Strait is a very dissipative environment. Almost all tidal energy, 85% or more for all considered cases, is lost within the Strait. The distribution of the rate of energy dissipation due to bottom friction implies that the major area of dissipation is located between Perim Narrows and the Assab-Mocha line.

In conclusion, the model results presented here and analyses of the available observations (Vercelli, 1925, 1927; Siedler, 1969; Jarosz, 2002) have significantly improved our understanding of the tidal frequency motion and its importance for the observed circulation in the Bab el Mandab Strait; however, they have also brought to light several topics that need to be addressed in the future. The most urgent of these is to develop an understanding of the baroclinic tidal motion and how this motion interacts with water mass exchange between the Red Sea and Gulf of Aden/Indian Ocean. Future work then will focus on internal tides and the application of a baroclinic model would be a useful tool to help understand their generation, propagation, and dissipation in this region.

References

Blain, C.A., Rogers, W.E., 1998. Coastal Tide Prediction Using the ADCIRC-2DDI Hydrodynamic Finite Element Model: Model Validation and Sensitivity Analyses in the Southern North Sea/English Channel. Formal Report NRL/FR/ 7322-98-9682. Naval Research Laboratory, Stennis Space Center, MS 92pp.

Brink, K.H., 1995. Tidal and lower frequency currents above Fieberling Guyot. Journal of Geophysical Research 100, 10,817–10,832.

Davies, A.M., Kwong, S.C.M., Flather, R.A., 1997. A three-dimensional model of diurnal and semi diurnal tides on the European shelf. Journal of Geophysical Research 102, 8625–8656.

Defant, A., 1961. Physical Oceanography. Pergamon Press, Oxford 598pp.

Foreman, M.G.G., 1977. Manual for tidal heights analysis and prediction. Pac. Mar. Sci. Rep. 77-10. Institute of Ocean Sciences, Patricia Bay, BC, Canada 101pp.

Foreman, M.G.G., 1978. Manual for Tidal Currents Analysis and Prediction. Pac. Mar. Sci. Rep. 76-6. Institute of Ocean Sciences, Patricia Bay, BC, Canada 70pp.

Foreman, M.G.G., Walters, R.A., Henry, R.F., Keller, C.P., Dolling, A.G., 1995. A tidal model for eastern Juan de Fuca

Strait and the southern Strait of Georgia. Journal of Geophysical Research 100, 721–740.

Gill, A.E., 1982. Atmosphere-Ocean Dynamics. Academic Press, New York 662pp.

Grenier, R.R., Luettich, R.A., Westerink, J.J., 1995. A comparison of the nonlinear frictional characteristics of two-dimensional and three-dimensional models of a shallow tidal embayment. Journal of Geophysical Research 100, 13,719–13,735.

Hendershott, M.C., 1981. Long waves and ocean tides. Evolution of Physical Oceanography. MIT Press, Cambridge, MA, pp. 292–341.

International Hydrographic Organization (IHO), Tidal Constituent Bank, 1979. Station Catalogue. Ocean and Aquatic Sciences, Dept. of Fisheries and Oceans, Ottawa, Canada.

Jarosz, E., 2002. Tidal dynamics in the Bab el Mandab Strait. Ph.D. thesis, Louisiana State University, Baton Rouge, Louisiana.

Kolar, R.L., Gray, W.G., Westerink, J.J., Luettich, R.A., 1994. Shallow water modeling in spherical coordinates: equation formulation, numerical implementation, and application. Journal of Hydraulic Research 32, 3–24.

Kowalik, Z., Polyakov, I., 1998. Tides in the Sea of Okhotsk. Journal of Physical Oceanography 28, 1389–1409.

Kowalik, Z., Proshutinsky, A.Y., 1993. Diurnal tides in the Arctic Ocean. Journal of Geophysical Research 98, 16,449–16,469.

Le Provost, C., Genco, M.L., Lyard, F., Vincent, P., Canceil, P., 1994. Spectroscopy of the world ocean tides from a finite element hydrodynamics model. Journal of Geophysical Research 99, 24,777–24,797.

Luettich, R.A., Westerink, J.J., Scheffner, N.W., 1992. ADCIRC: an advanced three-dimensional circulation model for shelves, coasts and estuaries, Report 1: theory and methodology of ADCIRC-2DDI and ADCIRC-3DL. Dredging Research Program Technical Report DRP-92-6, US Army Engineers Waterways Experiment Station, Vicksburg, MS, 137pp.

Lynch, D.R., Gray, W.G., 1979. A wave equation model for finite element tidal computations. Computers and Fluids 7, 207–228.

Munk, W., 1997. Once again: once again—tidal friction. Progress in Oceanography 40, 7–35.

Murray, S.P., Johns, W., 1997. Direct observations of seasonal exchange through the Bab el Mandab Strait. Geophysical Research Letters 24, 2557–2560.

Naval Oceanographic Office (NAVOCEANO), 1997. Data base description for Digital Bathymetric Data Base-Variable Resolution (DBDB-V), Version 1.0. Internal Report, Naval Oceanographic Office, Stennis Space Center, MS.

Pugh, D.T., 1987. Tides, Surges and Mean-Sea Level. Wiley, New York 486pp.

Reid, R.O., Herbich, J. (Eds.), 1990. Handbook of Coastal and Ocean Engineering. Gulf Publishing, Houston, TX.

Schwiderski, E.W., 1980. On charting global ocean tides. Reviews in Geophysics 18, 243–268.

Siedler, G., 1969. On the fine structure of density and current distribution and its short-time scale in different areas. Progress in Oceanography 5, 81–94.

Smeed, D., 1997. Seasonal variation of the flow in the Strait of Bab el Mandeb. Oceanologica Acta 20, 773–781.

Thompson, E.F., 1939. Chemical and physical investigations. The exchange of the water between the Red Sea and the Gulf of Aden over the "Sill". John Murray Expedition 1933-34, Scientific Reports, vol. 2, 105pp.

Tsimplis, M.N., Proctor, R., Flather, R.A., 1995. A two-dimensional tidal model for the Mediterranean Sea. Journal of Geophysical Research 100, 16,223–16,239.

Vercelli, F., 1925. Richerche di oceanografia fisica eseguite della R. N. AMMIRAGILIO MAGNAGHI (1923-24), Part I, Correnti e mare. Annali Idrografici 11, 1–188.

Vercelli, F., 1927. Richerche di oceanografia fisica eseguite della R. N. AMMIRAGILIO MAGNAGHI (1923-24), Part IV, La temperatura e la salinita. Annali Idrografici 11, 1–66.

Vercelli, F., 1931. Le Nuove recherche sulli correnti marine nel Mar Rosso. Annali Idrografici 12, 1–74.

Wahr, J., 1981. Body tides on an elliptical, rotating, elastic and oceanless Earth. Geophysical Journal of Royal Astronomical Society 64, 677–703.

Walters, R.A., 1987. A model for tides and currents in the English Channel and southern North Sea. Advances in Water Resources 10, 138–148.

Walters, R.A., Werner, F.E., 1989. A comparison of two finite element models of tidal hydrodynamics using a North Sea data set. Advances in Water Resources 12, 84–93.

Werner, F.E., Lynch, D.R., 1987. Field verification of wave equation tidal dynamics in the English Channel and southern North Sea. Advances in Water Resources 10, 115–130.

Westerink, J.J., Luettich, R.A., Baptista, A.M., Scheffner, N.W., Farrar, P., 1992. Tides and storm surge predictions using a finite element model. Journal of Hydraulic Engineering 118, 1373–1390.

Westerink, J.J., Blain, C.A., Luettich, R.A., Scheffner, N.W., 1994. ADCIRC: an advanced three-dimensional circulation model for shelves, coasts and estuaries; Report 2: users manual for ADCIRC-2DDI. Dredging Research Program Technical Report DRP-92-6, US Army Engineers Waterways Experiment Station, Vicksburg, MS, 156pp.

Westerink, J.J., Stolzembach, K.D., Connor, J.J., 1989. General spectral computations of the nonlinear shallow water tidal interactions within the Bight of Abaco. Journal of Physical Oceanography 19, 1350–1373.

Zimmerman, J.T.F., 1978. Topographic generation of residual circulation by oscillatory (tidal) current. Geophysical and Astrophysical Fluid Dynamics 11, 35–47.